Equatorial anisotropy in the inner part of Earth's inner core from autocorrelation of earthquake coda

Tao Wang[1,2], Xiaodong Song[1,2]* and Han H. Xia[1]

The Earth's solid inner core exhibits strong anisotropy[1-5], with wave velocity dependent on the direction of propagation due to the preferential alignment of iron crystals[6]. Variations in the anisotropic structure, laterally and with depth[7-11], provide markers for measuring inner-core rotation[12] and offer clues into the formation and dynamics of the inner core[13,14]. Previous anisotropy models of the inner core have assumed a cylindrical anisotropy in which the symmetry axis is parallel to the Earth's spin axis. An inner part of the inner core with a distinct form of anisotropy has been suggested[15], but there is considerable uncertainty regarding its existence and characteristics[16-19]. Here we analyse the autocorrelation of earthquake coda measured by global broadband seismic arrays between 1992 and 2012, and find that the differential travel times of two types of core-penetrating waves vary at low latitudes by up to 10 s. Our findings are consistent with seismic anisotropy in the innermost inner core that has a fast axis near the equatorial plane through Central America and Southeast Asia, in contrast to the north–south alignment of anisotropy in the outer inner core. The different orientations and forms of anisotropy may represent a shift in the evolution of the inner core.

Recent studies show that core phases can be retrieved by stacking cross-correlations of ambient noise[20-22] or earthquake coda[23] between seismic stations. We used a new technique similar to that in ref. 23 but applied to single-station autocorrelations (Methods). We observed clear inner-core arrivals PKIKP[2] and PKIIKP[2] (hereafter referred to as I2 and II2 phases, respectively) in the stacked empirical Green's functions (EGFs) at 57 arrays (Fig. 1 and Supplementary Figs 1–5). For an earthquake source, the I2 phase is a PKIKP phase (a compressional wave traversing the inner core) that is reflected at the Earth's surface and continues as another PKIKP phase to arrive at a receiving station. The II2 phase traverses the top of the inner core and has additional underside reflections at the inner-core boundary (ICB). In this study, the source and the receiver are at exactly the same location; that is, they have zero offset between them or the corresponding PKIKP and PKIIKP phases are at exactly 180° between the source (or the receiver) and its antipode, and thus the ray paths of the I2 (or II2) phase at a station and its antipode are exactly the same.

As a result of the weak reflection at the ICB, the PKIIKP phase (not to mention the II2 phase) is generally not observable from earthquakes unless at near-antipodal distances with the focusing effect[24,25]. Our technique instantly creates perfect round-trip arrivals at zero offset and antipodal geometries of the I2 phase (passing straight through the centre of the Earth) and the II2 phase (underside reflection at the ICB) from any arrays around the world (Fig. 1b) without the limitation of earthquake sources. The new type of data offers several advantages over traditional earthquake data. First,

Green's function (representing the response from an impulsive point source at the surface) is obtained if the noise field is fully diffuse[26], which allows us to stack directly individual autocorrelations from different time periods without the complications of variable source spectra and time functions. Second, our stacked EGFs indeed show great waveform similarity (Fig. 1c and Supplementary Figs 3–5), allowing us to measure relative times between different arrays much more precisely (Methods). Third, the similarity of the ray paths of PKIKP and PKIIKP (Fig. 1a) has allowed the authors of ref. 25 to rule out the effects from mantle heterogeneity, the Earth's ellipticity, and the ICB topography on producing large PKIIKP–PKIKP anomalies. Fourth, the II2–I2 time is twice the PKIIKP–PKIKP time, making anomalies easier to observe. We are not aware of any simultaneous observation of the I2 and II2 phases from an earthquake.

To examine the inner-core anisotropy, we define two angles ξ_p and ξ_e from the spin axis (the polar direction) and an axis near the Equator, respectively (Fig. 1d). For a cylindrical anisotropy, the compressional velocity perturbation can be expressed as[5,11]

$$\frac{\delta V}{V} = \alpha + \varepsilon \cos^2 \xi + \gamma \sin^2 2\xi$$

where ξ is the ray angle from the symmetry axis (that is, ξ_p or ξ_e), α is a baseline correction, and ε and γ are anisotropy parameters, which are related to elastic constants by: $\varepsilon = (C_{33} - C_{11})/2C_{11}$ and $\gamma = (4C_{44} + 2C_{13} - C_{11} - C_{33})/8C_{11}$.

We observed large variations (up to 10 s) in the II2–I2 residuals (relative to the average; Fig. 2), which are clearly visible in the original waveforms (Fig. 1c and Supplementary Figs 4 and 5). The decreasing trend of the residuals with ξ_p at mid- and high latitudes ($\xi_p < 60°$) can be well fitted by a cylindrical anisotropy model around the spin axis. The data agree with the predictions for an average seismic model for the outer inner core[11] (OIC) or a hexagonal close-packed (hcp) iron for the inner core[27], which fits well seismic data sampling the outer part of the inner core. However, at low latitudes ($\xi_p > 60°$), the data show a huge scatter. In the example shown in Fig. 1c, the stations are at similar latitudes; however, the residuals between the arrays in Central America (CAM) and in East Africa differ by as much as 9 s. The absolute arrival times of II2 differ only by a small amount, suggesting that most of the anomalies come from the I2 phase. The residuals in CAM and Southeast Asia are as large as those in Antarctica (Supplementary Fig. 5). Such large anomalies and variations from 'equatorial' paths have never been observed before[5] for the outer part of the inner core, which is much better sampled; thus, the main signal is probably from the deeper inner core.

We attempted to explain the equatorial data with a cylindrical anisotropy model. The anisotropy of the outer part of the inner core exhibits significant lateral variation, in particular, the hemispherical

[1]Institute of Geophysics and Geodynamics, and State Key Laboratory for Mineral Deposits Research, School of Earth Sciences and Engineering, Nanjing University, Nanjing, Jiangsu 210046, China. [2]Department of Geology, University of Illinois at Urbana-Champaign, Champaign, Illinois 61820, USA. *e-mail: xiao.d.song@gmail.com
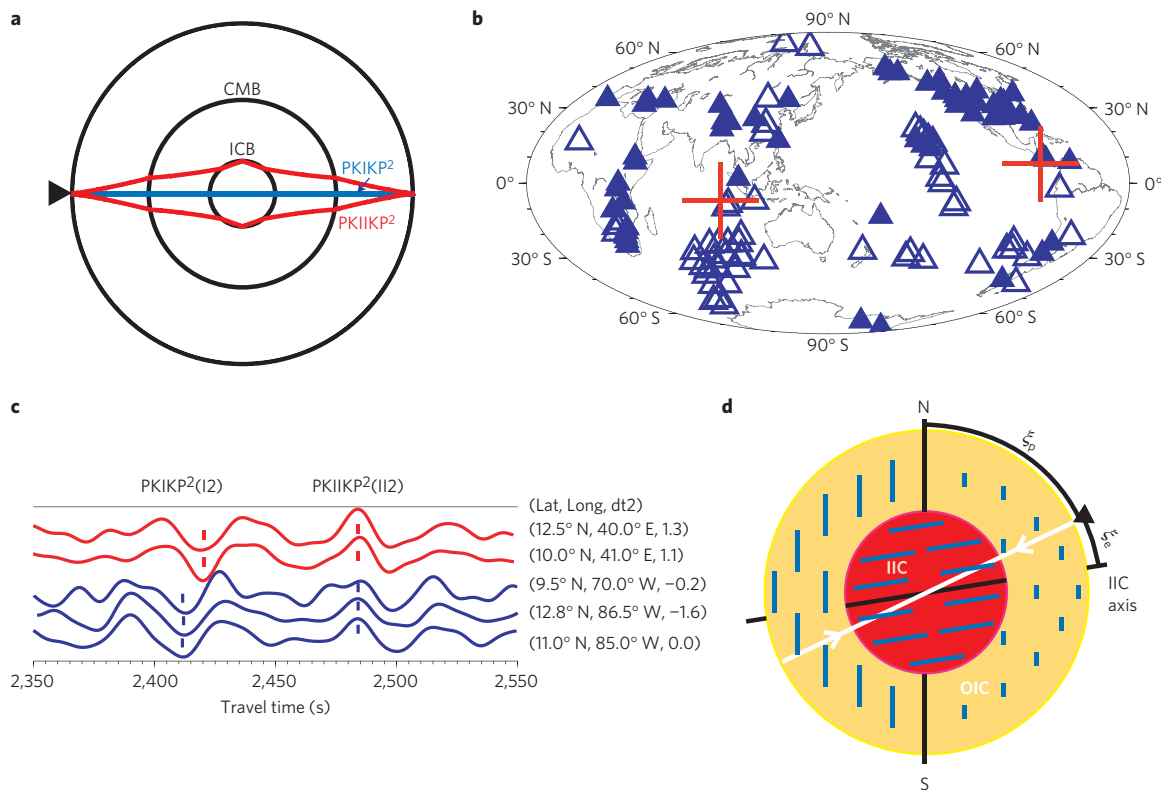
Figure 1 | Illustration of data used in this study. a, Ray paths of I2 and II2 waves from a station to its antipode and back. CMB, core–mantle boundary. **b**, Locations of 57 station arrays (filled triangles) and antipodes (open triangles) and the IIC fast axis (red crosses). **c**, Example EGFs from autocorrelation stacks. The blue and red traces are from arrays in CAM and East Africa, respectively (similar latitudes, location labelled). The ticks show the time picks of the I2 and II2 phases. The traces are shifted slightly (by dt2 in seconds) to align with the II2 phase of the last trace. **d**, Schematic of our model for the anisotropy of the OIC and the IIC (with a radius of about half the inner-core radius). The short sticks indicate the fast direction and the strength of the anisotropy. The angles of the I2 ray (white) at the station (black inverse triangle) from the spin axis and the equatorial IIC axis are represented by ξ_p and ξ_e, respectively.
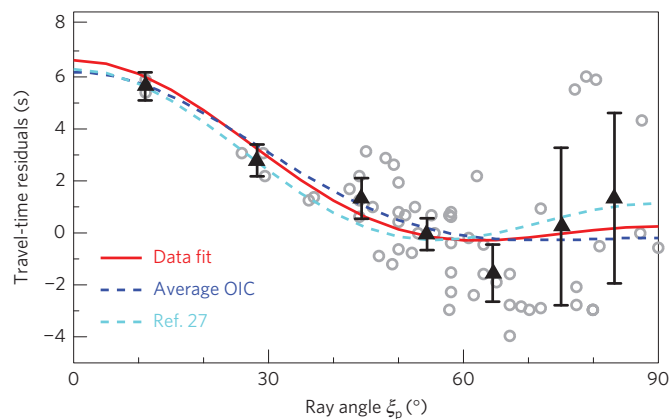

Figure 2 | Residuals of II2–I2 differential times (open circles) versus ray angle from the spin axis and best-fit cylindrical anisotropy model (red curve). Diamond and error bar are the mean and the ± one standard deviation of the mean over about 10° ray-angle interval. Shown in comparison are predictions for the average OIC from ref. 11 (blue dashed line) and the hcp iron model of ref. 27 (cyan dashed line), which are shifted and scaled to fit roughly the amplitude of the data variation. The OIC model is the longitudinal average of the three-dimensional model[11] from the ICB to the radius of 600 km.

variation[9,10], which needs to be corrected for the understanding of the deeper part. We used the three-dimensional inner-core anisotropy model from refs 11,18, which shows a sudden change in the anisotropy form from an OIC to an inner inner core (IIC) at slightly less than half of the inner-core radius (about 600 km). As any of our I2 arrivals would sample both hemispheres and the trend of our data at mid- and high latitudes agrees well with a longitudinally averaged OIC model ($\varepsilon = 1.862\%$, $\gamma = -0.583\%$) based on ref. 11, we used the average model to correct the residuals for the OIC to examine the remaining contributions for the IIC. The corrections have little effect on low-latitude stations ($\xi_p > 45°$). We did not apply any correction to the II2 phase, which samples the very shallow part (top 75 km) of the inner core with weak anisotropy[7,8]. The focusing effect at zero offset with rays arriving at all azimuths also provides a lateral averaging of the shallow inner core.

We searched for the best-fit symmetry axis and cylindrical anisotropy to the corrected data. If we use only the arrays at low latitudes (<45°; a total of 45 arrays), the best-fit axis is located at (9° N, 85° W) or its antipode at (9° S, 95° E). The anisotropy coefficients are $\varepsilon = 2.16\%$ and $\gamma = -2.08\%$ averaging over the IIC. The model fits the data remarkably well (Fig. 3a) and reduces the data variance by 78%. The model predicts the slowest value at $\xi_e = 53°$, which is about 3.3% slower than along the axis. If we use all of the data (including the polar paths), the best-fit axis is located at (9° N, 89° W) or its antipode at (9° S, 91° E) and the anisotropy coefficients are $\varepsilon = 1.71\%$ and $\gamma = -1.95\%$. The fast axis is about 2.9% faster than the slowest directions at $\xi_e = 51°$. The model, comparable to that using the low-latitude data alone, fits the trend of all the data (Fig. 3b) with a variance reduction of 64%. This is again remarkable, given the inevitable errors from the complex OIC anisotropy (particularly for the polar paths) in our corrections. Using a bootstrapping of all the data, we found that the location of
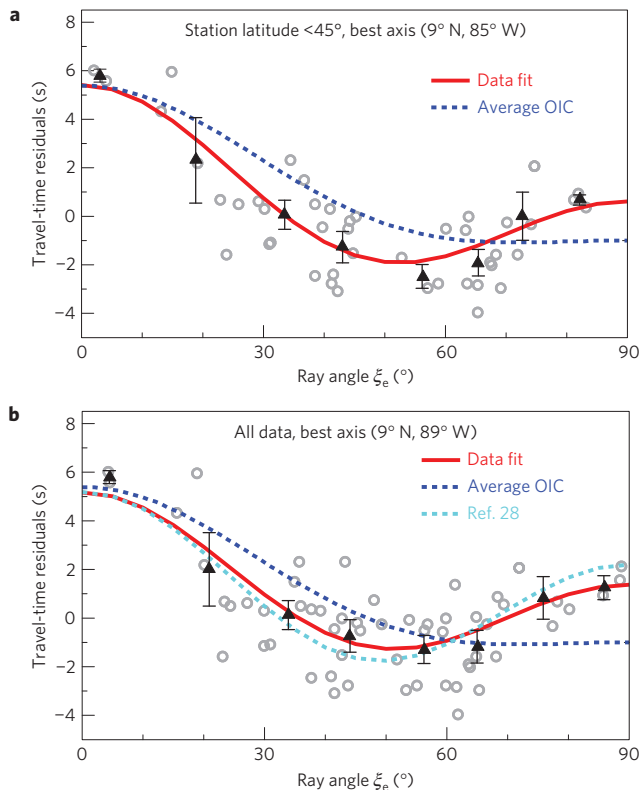
Figure 3 | Residuals of II2–I2 differential times (open circles) versus ray angle from the best-fit IIC axis. a,b, The residuals are corrected for the average OIC anisotropy of ref. 11, and the best-fit cylindrical anisotropy models (red curves) are derived from the low-latitude (less than 45°) arrays alone (**a**) and all of the data (**b**) respectively. Diamond and error bar are the mean and the ± one standard deviation of the mean over about 10° ray-angle interval. The best-fit axis for each case is indicated. Shown in comparison are predictions (scaled to fit roughly the amplitude) for the average OIC model (blue dashed line) in **a** and **b** and the bcc iron model in ref. 28.

the fast axis for the IIC is confined to latitude (6° N to 12° N) and longitude (83° W to 95° W) (off the coast of Costa Rica in the Pacific Ocean) or their antipodes (off the coast of Sumatra in the Indian Ocean) at the 95% confidence level.

The predicted pattern of travel-time residuals from the combined (OIC + IIC) model matches well the overall pattern of the observations (Fig. 4). There are two fast axes: the spin axis, which is fastest for the OIC and relatively fast for the IIC, and the axis for the IIC, which is tilted slightly (9°) from the equatorial plane. The combined model predicts two rings of negative residuals, corresponding to the arrays in East and South Africa, Taiwan, Tibet, Hawaii and South America. The rings are 'broken' asymmetrically at high latitudes because of the slight tilt of the fast axis from the Equator, and thus the residuals of US arrays (or their antipodal projections) show a complex pattern with values generally higher than in other regions of similar latitudes. Using earthquakes recorded by arrays in Venezuela and Southeast China at near-antipodal distances, the authors of ref. 25 found that the Venezuela path is about 1.8 s larger in the PKIIKP–PKIKP differential times. Our model prediction is in excellent agreement (1.5 and 2.0 s for the two IIC models, respectively). We also note that the systematic trend (Fig. 3) and the general pattern (Fig. 4) of the data argue against a very local heterogeneity; for example, a very fast anomaly under the CAM or the Southeast Asia would affect only the two regions. The velocity variation with the ray angle depends on the ratio[18] $\kappa = -\gamma / \varepsilon$. The dependency for the OIC is well observed[5,18]:

the velocity varies very little at large ray angles ($\kappa = 0.31$ for the OIC model in Fig. 3). The κ ratios for our IIC models are 0.96 and 1.14, respectively, resulting in the slowest direction at an intermediate ray angle and large variations even at intermediate and large ray angles.

The basic features of our models for the IIC described above are highly robust (see Methods and Supplementary Information for detailed discussion of data and model uncertainties), although details may change with additional observations and improved waveform-based modelling techniques. We examined several models for the OIC corrections (Supplementary Section 3 and Supplementary Fig. 14). The results are all quite similar to the models above and well within the error bounds (Supplementary Fig. 15). This is due to the averaging effect of the I2 ray over three-dimensional inner-core anisotropy with the dominant hemispherical pattern. At long periods (20–40 s) of our EGFs, the Fresnel zones of I2 and II2 in the inner core are large so that the II2 phase may be affected by strong anisotropy at greater depth of the OIC. We argue, however, that the effect on the low-latitude stations is probably small and would not change our basic conclusions on the equatorial axis and the distinct form of the IIC anisotropy (Supplementary Section 4).

There are considerable uncertainties in the crystal structure of iron in the inner core with the hcp (refs 6,27) or body-centred cubic[28,29] (bcc) structure being favoured, the mechanism for its preferred orientation, and the determination of elastic parameters. The separate trends of anisotropy are in good agreement with the hcp iron of ref. 27 (aligned in the *c* axis) in the OIC (Fig. 2) and the bcc iron of ref. 28 (aligned with the main diagonal [111] axis) in the IIC (Fig. 3), respectively, but not vice versa. The two-phase (hcp–bcc) system of iron in the inner core is consistent with a first-principle calculation[29]. Our models suggest that the IIC anisotropy is about 70% stronger than the OIC. The change in shape and strength of the anisotropy from the IIC to the OIC may represent a tectonic evolution of the inner core[13] and thus our finding may indeed offer 'clues about the inner-core history: its age, thermal process, and possibly an early convective event'.

Methods

Retrieval of EGFs. We systematically processed 20 years (1992–2012) of global broadband arrays using coda waves of earthquakes with magnitude 7 or greater to obtain our EGFs. Our original data were from the Incorporated Research Institutions for Seismology (IRIS) Data Management Center (DMC), which included dense arrays of global permanent stations and temporary deployments (broadband vertical component; Supplementary Fig. 1 and Table 1). The data
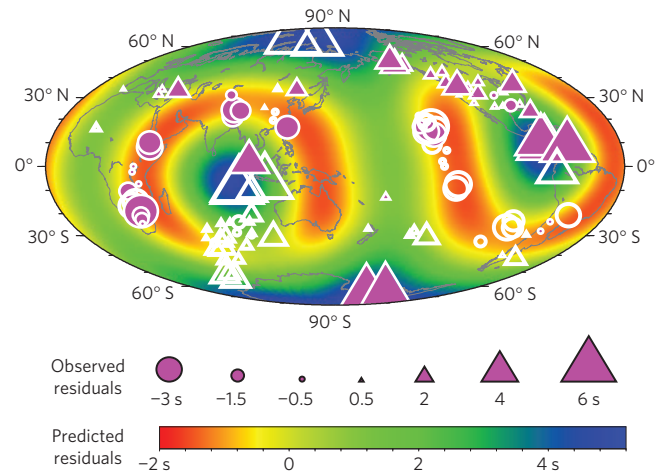

Figure 4 | Residuals of observed II2–I2 differential times (symbols) and model global predictions (colour background). The predictions are based on the combination of the average OIC model of ref. 11 and our best-fit IIC model using all of the data. Observed residuals are plotted at the array locations (filled symbols) and their antipodes (open symbols).

duration ranges from 1 to 13 years (most arrays span from 2005 to 2012). We selected a total of 57 dense arrays, which, together with their antipodes, provide a good global coverage (Fig. 1b). The total number of stations used in this study is 1,797. The number of stations in each array ranges from 4 (in Antarctica) to 144 (in the US), with most larger than 17 (68%). The size of each array ranges from 0.8° to 5° with most around 2° (74%), depending on the density of available stations.

We computed single-station autocorrelations to retrieve the EGFs of I2 and II2 phases. We used a procedure similar to the cross-correlation technique in ref. 23. First, to obtain a high enough signal-to-noise ratio of autocorrelations, we discarded stations that recorded fewer than 10 large earthquakes (magnitude ≥ 7). Second, we decimated the sampling rate to 0.2 s and then cut the time segment of the coda (10,000–30,000 s) after a large earthquake (magnitude ≥ 7). Third, we implemented a band-pass filter (15∼50 s) for all data to retain the dominant frequency of large earthquakes and to reduce the influence of surface noises. Last, following a procedure similar to that in ref. 30, we applied time domain normalization with the running absolute mean to reduce the effect of energetic sources, applied spectral whitening, and calculated the autocorrelation for each station.

To enhance further the signal-to-noise ratio, we stacked stations within a certain aperture of a given array (Supplementary Fig. 1). We chose the centre and the aperture on the basis of the density of available stations for the array. For example, the aperture is 1° for a dense array in the western US (our master array has 67 stations). On the other hand, the aperture is 5° for the Antarctic arrays because of the sparse station distribution. We performed the stacking in two steps. First, we stacked all of the available traces to obtain an initial stacked trace. Second, we discarded bad traces if the correlation coefficient between the trace and the initial stacked trace is less than 0.5 or if the delay time of the maximum correlation is larger than 7 s. We then stacked the remaining traces to obtain the final array stack.

We examined the accuracy of our retrieved EGFs, including several tests on division of seismicity, array location, time windows after the earthquakes, type of body waves, and numbers of stations and events (Supplementary Section 1 and Supplementary Figs 6–10). The results suggest that the EGFs are unlikely to be biased by the heterogeneity of earthquake distribution and most of our EGFs are robust. Most of the energy contributing to the autocorrelations comes from the time window 10,000–40,000 s after major earthquakes, consistent with the cross-correlation study in ref. 23. The errors of the II2–I2 differential-time measurements for most arrays (80%) are probably less than 1.3 s.

Measurements of II2–I2 differential travel times. We measured the relative times of the same phase (I2 or II2) between different traces using a semi-automatic procedure of waveform cross-correlations, visual inspection, and hand picking. We chose a stacked trace from a dense array in the western US (Array 7 in Supplementary Fig. 1) as the master trace (Supplementary Fig. 2) and hand picked its I2 and II2 arrival times. We first relied on automatic waveform cross-correlation to measure the relative time between a trace and the master trace for the same phase. As we are interested in only relative times (between I2 and II2) and differences in the relative times (between different arrays), using waveform cross-correlation is much more precise than hand picking. Most of the stacked waveforms are very similar (Supplementary Figs 3 and 4); thus, we fixed the correlation time windows for the I2 and II2 phases at 2,370–2,440 s and 2,470–2,500 s, respectively, for all of the cross-correlation measurements. We visually inspected every correlation pick. For some traces whose waveforms differ slightly, we used visual alignments relative to the master trace to pick the arrival times (including 13 picks for the I2 phase and 18 picks for the II2 phase). Last, we defined the differential-time residuals as the measured II2–I2 times minus the average of all the measurements (66.5 s). A more detailed discussion on the travel-time measurements and the influence of measurement uncertainties can be found in Supplementary Section 2 and Supplementary Figs 11–13. If we leave out some of the poorer quality data, the best-fit models differ little from the original models.

Data. The data for this study were from IRIS DMC (see Supplementary Table 1 for detailed information).

References

1. Morelli, A., Dziewonski, A. M. & Woodhouse, J. H. Anisotropy of the inner core inferred from PKIKP travel times. *Geophys. Res. Lett.* **13,** 1545–1548 (1986).
2. Woodhouse, J. H., Giardini, D. & Li, X. D. Evidence for inner core anisotropy from free oscillations. *Geophys. Res. Lett.* **13,** 1549–1552 (1986).
3. Creager, K. C. Anisotropy of the inner core from differential travel times of the phases PKP and PKIKP. *Nature* **356,** 309–314 (1992).
4. Tromp, J. Support for anisotropy of the Earth's inner core from free oscillations. *Nature* **366,** 678–681 (1993).
5. Song, X. D. Anisotropy of the Earth's inner core. *Rev. Geophys.* **35,** 297–313 (1997).
6. Brown, J. M. & Mcqueen, R. G. Phase transitions, Grüneisen parameter, and elasticity for shocked iron between 77 GPa and 400 GPa. *J. Geophys. Res.* **91,** 7485–7494 (1986).
7. Shearer, P. M. Constraints on inner core anisotropy from PKP(DF) travel times. *J. Geophys. Res.* **99,** 19647–19659 (1994).
8. Song, X. D. & Helmberger, D. V. Depth dependence of anisotropy of Earth's inner core. *J. Geophys. Res.* **100,** 9805–9816 (1995).
9. Tanaka, S. & Hamaguchi, H. Degree one heterogeneity and hemispherical variation of anisotropy in the inner core from PKP(BC)–PKP(DF) times. *J. Geophys. Res.* **102,** 2925–2938 (1997).
10. Niu, F. L. & Wen, L. X. Hemispherical variations in seismic velocity at the top of the Earth's inner core. *Nature* **410,** 1081–1084 (2001).
11. Sun, X. L. & Song, X. D. Tomographic inversion for three-dimensional anisotropy of Earth's inner core. *Phys. Earth Planet. Inter.* **167,** 53–70 (2008).
12. Song, X. D. & Richards, P. G. Seismological evidence for differential rotation of the Earth's inner core. *Nature* **382,** 221–224 (1996).
13. Deguen, R. & Cardin, P. Tectonic history of the Earth's inner core preserved in its seismic structure. *Nature Geosci.* **2,** 418–421 (2009).
14. Alboussiere, T., Deguen, R. & Melzani, M. Melting-induced stratification above the Earth's inner core due to convective translation. *Nature* **466,** 744–747 (2010).
15. Ishii, M. & Dziewonski, A. M. The innermost inner core of the earth: Evidence for a change in anisotropic behavior at the radius of about 300 km. *Proc. Natl Acad. Sci. USA* **99,** 14026–14030 (2002).
16. Beghein, C. & Trampert, J. Robust normal mode constraints on inner-core anisotropy from model space. *Science* **299,** 552–555 (2003).
17. Cormier, V. F. & Stroujkova, A. Waveform search for the innermost inner core. *Earth Planet. Sci. Lett.* **236,** 96–105 (2005).
18. Sun, X. L. & Song, X. D. The inner inner core of the Earth: Texturing of iron crystals from three-dimensional seismic anisotropy. *Earth Planet. Sci. Lett.* **269,** 56–65 (2008).
19. Lythgoe, K. H., Deuss, A., Rudge, J. F. & Neufeld, J. A. Earth's inner core: Innermost inner core or hemispherical variations? *Earth Planet. Sci. Lett.* **385,** 181–189 (2014).
20. Lin, F. C. et al. Extracting seismic core phases with array interferometry. *Geophys. Res. Lett.* **40,** 1049–1053 (2013).
21. Nishida, K. Global propagation of body waves revealed by cross-correlation analysis of seismic hum. *Geophys. Res. Lett.* **40,** 1691–1696 (2013).
22. Boue, P. et al. Teleseismic correlations of ambient seismic noise for deep global imaging of the Earth. *Geophys. J. Int.* **194,** 844–848 (2013).
23. Lin, F. C. & Tsai, V. C. Seismic interferometry with antipodal station pairs. *Geophys. Res. Lett.* **40,** 4609–4613 (2013).
24. Rial, J. A. & Cormier, V. F. Seismic waves at the epicenter's antipode. *J. Geophys. Res.* **85,** 2661–2668 (1980).
25. Niu, F. L. & Chen, Q. F. Seismic evidence for distinct anisotropy in the innermost inner core. *Nature Geosci.* **1,** 692–696 (2008).
26. Weaver, R. L. & Lobkis, O. I. Diffuse fields in open systems and the emergence of the Green's function. *J. Acoust. Soc. Am.* **116,** 2731–2734 (2004).
27. Stixrude, L. & Cohen, R. E. High-pressure elasticity of iron and anisotropy of Earth's inner core. *Science* **267,** 1972–1975 (1995).
28. Mattesini, M. et al. Hemispherical anisotropic patterns of the Earth's inner core. *Proc. Natl Acad. Sci. USA* **107,** 9507–9512 (2010).
29. Belonoshko, A. B., Skorodumova, N. V., Rosengren, A. & Johansson, B. Elastic anisotropy of Earth's inner core. *Science* **319,** 797–800 (2008).
30. Bensen, G. D. et al. Processing seismic ambient noise data to obtain reliable broad-band surface wave dispersion measurements. *Geophys. J. Int.* **169,** 1239–1260 (2007).

Author contributions

X.S. designed the project, performed data analysis, and wrote the paper. T.W. carried out data processing, performed data analysis, and contributed to the paper writing. H.H.X. contributed to data processing.

Additional information

Supplementary information is available in the online version of the paper. Reprints and permissions information is available online at www.nature.com/reprints. Correspondence and requests for materials should be addressed to X.S.

Competing financial interests

The authors declare no competing financial interests.